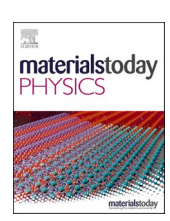
ELSEVIER

Contents lists available at ScienceDirect

Materials Today Physics

journal homepage: www.journals.elsevier.com/materials-today-physics





Spin-phonon interactions induced anomalous thermal conductivity in nickel (II) oxide

Qiyang Sun ^a, Songrui Hou ^b, Bin Wei ^{a,c}, Yaokun Su ^b, Victor Ortiz ^a, Bo Sun ^d, Jiao Y.Y. Lin ^e, Hillary Smith ^f, Sergey Danilkin ^g, Douglas L. Abernathy ^h, Richard Wilson ^{a,*}, Chen Li ^{a,b,**}

- ^a Mechanical Engineering, University of California, Riverside, Riverside, CA, 92521, USA
- ^b Materials Science and Engineering, University of California, Riverside, Riverside, CA, 92521, USA
- c Henan Key Laboratory of Materials on Deep-Earth Engineering, School of Materials Science and Engineering, Henan Polytechnic University, Jiaozuo, 454000, China
- ^d Tsinghua-Berkeley Shenzhen Institute and Guangdong Provincial Key Laboratory of Thermal Management Engineering and Materials, TSIGS, Tsinghua University, Shenzhen, 518055, China
- ^e Neutron Data Analysis and Visualization Division, Oak Ridge National Laboratory, Oak Ridge, TN 37830, USA
- ^f Department of Physics and Astronomy, Swarthmore College, Swarthmore, PA, 19081, USA
- g Australian Centre for Neutron Scattering, Australian Nuclear Science and Technology Organization, Lucas Heights, NSW, 2234, Australia
- ^h Neutron Scattering Division, Oak Ridge National Laboratory, Oak Ridge, TN, 37830, USA

ARTICLE INFO

Keywords: Nickel oxide Spin-phonon interaction Magnon and phonon dynamics Magnon thermal conductivity Phonon thermal conductivity

ABSTRACT

Nickel (II) oxide is a prominent candidate for spintronic and spin-caloritronic applications operating at room temperature. Although there are extensive studies on nickel oxide, the roles of magnon- and spin-phonon interactions on thermal transport are not well understood. In the present work, the relationship between spin-phonon interactions and thermal transport is investigated by performing inelastic neutron scattering, time-domain thermoreflectance thermal conductivity measurements, and atomistic thermal transport calculations. Inelastic neutron scattering measurements of the magnon lifetime imply that magnon thermal conductivity is trivial, and so heat is conducted only by phonons. Time-domain thermoreflectance measurements of the thermal conductivity vs. temperature follow $T^{-1.5}$ in the antiferromagnetic phase. This temperature dependence cannot be explained by phonon-isotope and phonon-defect scattering or phonon softening. Instead, we attribute this to magnon-phonon scattering and spin-induced dynamic symmetry breaking. The spin-phonon interactions are saturated in the paramagnetic phase and lead to a weaker temperature dependence of $T^{-1.0}$ at 550–700 K. These results reveal the importance of spin-phonon interactions on lattice thermal transport, shedding light on the engineering of functional antiferromagnetic spintronic and spin-caloritronic materials through these interactions.

1. Introduction

Thermal transports in magnetic insulators are predominantly governed by lattice dynamics, spin dynamics, and mutual interactions between them. Phonons and magnons are quantized energy carriers that correspond to lattice and spin degrees of freedom. Their contributions to thermal conductivity vary in different systems. Phonons usually carry most of the heat in magnetic insulators. Magnons also affect the thermal transport of magnetic insulators through two mechanisms. First, in some insulators, the amount of heat carried by magnons is comparable to that of phonons at low temperatures [1–5]. Second, spin-phonon interactions affect phonon energies and mean free paths, thus the transport of

phonons [6,7]. Although thermal conductivity governed by phonon-phonon scattering can be understood by the theory of lattice anharmonicity [8], the effects of magnon and spin-phonon interactions are less well understood [9]. The majority of existing work focused on tuning thermal conductivity by an external magnetic field at low temperatures, where thermal transport is not dominated by phonons. It was observed that with increasing external magnetic field, the magnon-phonon interaction is weakened and the thermal conductivity is enhanced in ferromagnetic, ferrimagnetic and magnetic frustrated materials [10–12]. These observations suggest that spin-phonon interactions suppress thermal transport. However, the thermal conductivity in antiferromagnetic materials has a much weaker field

 $^{^{\}ast}$ Corresponding author.

^{**} Corresponding author. Mechanical Engineering, University of California, Riverside, Riverside, CA, 92521, USA. *E-mail addresses*: rwilson@ucr.edu (R. Wilson), chenli@ucr.edu (C. Li).

dependence [6], thus the effects from spin-phonon interactions are not extensively explored. There are great potentials in engineering thermal transport through such interactions.

Antiferromagnetic (AFM) insulators exhibit characteristics of low damping and robustness against external magnetic perturbations, which make them promising candidate materials for quantum computing devices [13], ultrafast spintronics [14–17], memory devices [18], and spin-caloritronic applications [19,20]. Colinear AFM insulator nickel (II) oxide (NiO) is a prominent candidate for next-generation spintronic and spin-caloritronic applications operating at room temperature because it has high spin transport efficiency [21–24] and high Néel temperature ($T_N = 523 \; \text{K}$) [25–27], and its magnetic order can be manipulated by ultrafast photoexcitation [28]. Importantly, spin-induced dynamic symmetry breaking and the mutual spin-phonon driving effect have recently been reported in NiO, suggesting the presence of strong spin-phonon interactions may significantly affect phonon transport and motivates the current work.

While there are extensive experimental and theoretical studies on thermal transport in single crystal NiO [30–35], there are no conclusive experimental thermal conductivity data or atomistic models for magnon and phonon transport in the context of spin-phonon interactions. The most cited experimental work was done by F. B. Lewis et al. [32]. Although the thermal conductivity was reported to increase with temperature in the paramagnetic (PM) phase, suggesting strong spin-phonon interactions, the measurement was not conclusive because of possible radiational heat loss [32]. The increase of thermal conductivity in the PM phase is contrary to later measurements done by M. Massot et al. [34], who measured the thermal conductivity only in the vicinity of T_N. Moreover, characterizing the magnon and phonon dynamics is pivotal for investigating the effect of spin-phonon interactions. Previous Raman experiments only focused on the temperature dependence of the phonon energy at the zone center [36]. The lack of accurate measurements of thermal conductivity in a wide temperature range, characterizations of temperature-dependent magnon and phonon dynamics off zone centers, and atomistic models for magnon and phonon transport hindered further investigations of thermal transports in this important material. The present work sheds light on these points.

In the current work, we performed inelastic neutron scattering (INS) experiments to characterize magnon and phonon dynamics, time-domain thermoreflectance (TDTR) measurements to measure temperature-dependent thermal conductivity, and atomistic simulations to investigate phonon and magnon transport in the context of spin-phonon interactions in NiO. INS measurements of magnon lifetimes indicate that the magnon thermal conductivity is negligible at all temperatures. TDTR measurements reveal that the thermal conductivity of NiO decreases from $\sim 55~W/(m \bullet K)$ at 200 K to $\sim 13~W/(m \bullet K)$ at 500 K. First principles calculations show that this temperature dependence is greater than can be explained with phonon-phonon and phonon-defect scattering (from 53 to 20 $W/(m \bullet K)$ in the same temperature range). INS measurements of temperature-induced phonon energy softening cannot also explain the observed temperature dependence of thermal conductivity. We attribute the difference to spin-phonon interactions.

2. Methods

2.1. Experimental

2.1.1. INS experiments

Time-of-flight INS measurements were performed on single-crystal NiO with Wide Angular-Range Chopper Spectrometer (ARCS) at the Spallation Neutron Source at Oak Ridge National Laboratory. Incident energy of 150 meV was used for measurements under 10, 300, 540 and 640 K. The sample was loaded with Al foil and placed in a low-background electrical resistance vacuum furnace with (H,H, 0) plane horizontal. Data reduction was performed with MANTID [37]. The INS

data were normalized by the proton current on the target and corrected for detector efficiency using a vanadium scan. Since no detectable difference can be found in binning experimental data (10, 300 K) with distorted rhombohedral or FCC lattice coordinates, the slight structure distortion of the AFM phase was neglected, and the FCC crystal structure was used for data analysis. The data was sliced along high symmetry **Q**-directions in reciprocal space to produce two-dimensional energy-momentum views of dispersions.

Time-of-flight INS measurements were also performed on polycrystalline NiO. The sample was loaded in an Al sample can and mounted in a low-background electrical resistance vacuum furnace. The two-dimensional dynamic structure factors $S(|\mathbf{Q}|,E)$ were obtained at $T=50,\,280,\,450,\,540$ and 640 K using an incident energy of 50 and 150 meV. INS measurements on an empty Al can were performed at the same temperatures and neutron incident energy. The measured intensity, as the INS background induced by the sample holder, was subtracted from the polycrystalline data. The data have been corrected by multiphonon scattering and thermal occupation using Getdos [38].

Triple-axis INS measurements were performed on the same single-crystal with triple-axis spectrometer TAIPAN at OPAL reactor at ANSTO to map phonon dispersion near the zone center. Constant $\bf Q$ scans near zone centers at (1,1,1), (0,2,2) and (0,0,2), and constant energy scans at 10,15, and 20 meV along [1,1,1] were performed at 300, 450, and 650 K.

2.1.2. TDTR experiments

We performed TDTR measurements on two single-crystal NiO samples between 125 and 675 K. TDTR is a well-established pump probe technique for the characterization of thermal properties [39]. Details of our TDTR setup can be found in Ref. [40]. We mounted the samples in a heater stage (Microptik MHCS600) for temperatures above 300 K and in a cryostat (Janis ST-300MS) below 300 K. We pumped the sample chamber down to $\sim 10^{-5}$ torr during the experiments. We coated the NiO samples with a $\sim\!80$ nm Al film. The Al film serves as both a heat absorber and a thermometer. In TDTR measurements, a train of 783-nm-wavelength laser pulses emitted from a mode-locked Ti:sapphire oscillator is split into a pump beam and a probe beam. The pump beam heats the sample at a modulation frequency of 10.7 MHz. The probe beam monitors the temperature decay at the sample surface via temperature-induced changes in the reflectance of the Al film. The reflected probe beam from the Al film is collected by a silicon photodiode detector. A lock-in amplifier reads the microvolt change in voltage output by the detector due to changes in reflected probe beam intensity. The amplifier outputs the in-phase signal V_{in} and the out-of-phase signal Vout at the 10.7 MHz modulation frequency. The size of the laser spot in $1/e^2$ radius $w_0 = 6.5 \mu m$ and is measured by the beam offset method [41]. We controlled the steady-state temperature rise in NiO to be less than 5 K considering its phase transition at 523 K. The steady-state temperature increase in the TDTR measurements is [39].

$$\Delta T_s = \frac{P_i(1-R)}{2\sqrt{\pi}w_0\kappa},$$

where P_i is the incident laser power, R is the optical reflectivity of Al, and κ is the thermal conductivity of NiO. We make sure $\Delta T_s < 5$ K by controlling the incident pump and probe power.

We analyzed the collected ratio, $-V_{in}/V_{out}$, using a heat diffusion model to extract the thermal conductivity of NiO [39]. The model needs several input parameters, such as laser spot size, modulation frequency, and thermal properties of each layer. We measured the thickness of the Al film by picosecond acoustics [42]. We used experimental results from literature for the heat capacity of Al and NiO at different temperatures [32,43,44]. For the heat capacity of NiO above 630 K, there is no experimental data. Thus, we extrapolate the experimental results in Ref. [32].

2.1.3. INS data folding

Data folding was used to increase the counting statistics and remove the neutron scattering form factor in the dynamic structure factors $S(\mathbf{Q}, \mathbf{E})$. Data folding was done by summing up the $S(\mathbf{Q}, \mathbf{E})$ data from over 100 BZs into an irreducible wedge in the first Brillouin zone. The offsets of the q grids were corrected by fitting the measured Bragg diffractions. This folding technique has been used in a previous study [45] and has been demonstrated to be reliable.

2.2. Calculational

2.2.1. First-principles calculations and thermal conductivity simulations

The ab initio density functional theory (DFT) calculations were performed with the VASP (Vienna Ab initio Simulation Package) [46,47] on a plane wave basis set, using the projector augmented wave (PAW) pseudopotentials [48,49] with local spin density approximation (LSDA) exchange correlation functionals [50] and the Hubbard-U model [51]. U = 5 eV was chosen to obtain the best match with experimental phonon dispersion, although it underestimated the electron band gap [52]. An energy cutoff of 550 eV was used for all calculations. LSDA + U ionic relaxation was performed based on a primitive cell containing two nickel and two oxygen atoms with collinear antiferromagnetic (AFM) spin order. A Γ -centered k-point grid of $13 \times 13 \times 13$ was used in LSDA + U ionic relaxation. The relaxed cell has a slight contraction along the [1,1,1] direction. The calculated distortion angle of 0.15°, which deviates from 60° in the FCC primitive cell, is larger than the experiment value in Ref. [53]. The relaxed rhombohedral cell (space group 166) with a lattice constant of 4.958 Å and an angle of 33.66° (from an undistorted value of 33.55°) were used in the phonon dispersion calculations. The static dielectric tensor and Born effective charges were obtained to calculate nonanalytical terms in phonon calculations. The second order interatomic force constants were obtained from a $2 \times 2 \times 2$ supercell of 32 atoms with a Monkhorst-Pack k-point grid of $6 \times 6 \times 6$ using the density functional perturbation theory (DFPT). Phonon eigenvalues and eigenvectors were obtained by diagonalizing the dynamical matrix implemented in Phonopy [54].

Third-order force constants were also calculated using a $2 \times 2 \times 2$ supercell, corresponding to 32 atoms with $6 \times 6 \times 6$ reciprocal mesh sampling and an energy cutoff of 550 meV. The third-order force constants were calculated from 226 inequivalent displacements based on the supercell mentioned forehead without a pair-cutoff distance. Second-order and third-order force constants are symmetrized to minimize drift force constants as implemented in Phono3py [55]. Phonon lifetimes were obtained from the imaginary part of the calculated phonon self-energy, which was evaluated by the lowest-order many-body perturbation theory as implemented in Phono3py. The lattice thermal conductivity accounting for 3-phonon scattering was calculated by solving the linearized phonon Boltzmann equation (LBTE) using the single mode relaxation-time method [55,56] with Phono3py. The lattice thermal conductivity using the direct solution of LBTE is also calculated with Phono3py. Phonon lifetimes and lattice thermal conductivity converged in $20 \times 20 \times 20$ **q** mesh. The isotope scattering due to the mass variance of isotope distributions was performed as implemented in Phono3py. The thermal conductivity by phonon-phonon, phonon-isotope and phonon-defect scattering is estimated by $\kappa_{pd} = \frac{1}{N} \sum_{qi} c_{qj} v_{qj}^2 \tau_{p,qj}$.

According to Matthiessen's rule, the single-mode phonon relaxation time at specific q and branch j follows $\frac{1}{\tau_{p,qj}} = \frac{1}{\tau_{pp,qj}} + \frac{1}{\tau_{pl,qj}} + \frac{1}{\tau_{pl,qj}}$, where $\tau_{pp,qj}$, $\tau_{pi,qj}$ and $\tau_{pd,qj}$ stand for relaxation time by phonon-phonon, phononisotope and phonon-defect scattering. It is assumed that the relaxation time of the scattering of phonon defects due to point defects is assumed to follow $\tau_{pd,qj}^{-1}(\omega_{qj}) = A\left(\frac{\omega_{qj}}{\omega_{max}}\right)^4$, where A is a scaling factor; ω_{qj} and ω_{max} are the phonon energy and cutoff phonon energy at point q for branch j, respectively. A is obtained by fitting the measured thermal conductivity of NiO (I) below 200 K.

The phonon properties with collinear ferromagnetic (FM) spin order were calculated based on the same relaxed cell mentioned forehead. The second order force constants, the static dielectric tensor and Born effective charges were obtained in the same procedures. By changing from AFM to FM spin order, the phonon maximum energy increase 5.6%. The phonon Grüneisen parameters with FM and AFM spin order were calculated from three separate phonon band structure calculations with lattice constants of -0.3%, 0% and +0.3%, as implemented in *Phonopy*.

3. Result and discussion

Time-of-flight INS measurements were performed on single-crystal NiO with ARCS spectrometer at the Spallation Neutron Source (see Sec. 2.1.1). The four-dimensional dynamic structure factors, S (Q,E), were mapped at 10, 300, 540 and 640 K and folded into an irreducible wedge in one Brillouin zone (see Sec. 2.1.3). In Fig. 1, the folded S (Q,E) shows phonon and magnon dispersions. The spectral intensity of the magnons is weaker than that of the phonons. In Fig. 1 c, the measured phonon dispersion shown in the folded S (Q,E) is consistent with previous measurements at 300 K [57]. The S (Q,E) calculated by the coherent lattice INS (see SI note 1) at 10 K shows excellent agreement with the measurements (Fig. 1 a, b). Our DFT calculation predicts the longitudinal optic mode energy of 71.2 meV at the zone center (Γ), matching well with our measurement and previous Raman measurement at 300 K [36]. Two branches of nondispersive INS intensities around 23 and 35 meV overlay with low-lying optical modes (Fig. 1 b, c). These intensities arise from incoherent INS by nickel atoms, which have a non-trivial incoherent scattering cross section of 5.2 b. This is confirmed by the coherent one-phonon scattering dynamic structure factor simulation in Fig. 1 a. Similar incoherent scattering intensities have been observed in CoO [58]. Our INS measurements provide detailed characterizations of magnon and phonon properties and shed light on the calculation of thermal conductivity, as discussed below.

The total thermal conductivity (κ) in NiO can be represented as $\kappa = \kappa_m + \kappa_p$, where κ_m and κ_p are the thermal conductivity by magnon and phonon transports, respectively. In this system, the intrinsic linewidth broadenings of magnons were much smaller than the magnon energy. Magnons would be well defined and can be treated as propagating quasiparticles. In this case, the kinetic theory of thermal transport can be applied to calculate the magnon thermal conductivity [59]. The thermal conductivity along [1,0,0] can be calculated with

$$\kappa_m = \sum_q c_q v_q^2 \tau_q,$$

where c_q , v_q , τ_q are the mode volumetric specific heat (energy density per unit volume), projected group velocity along the [1,0,0] direction and the mode relaxation time of magnon at the grid point q, respectively. The c_q takes the form,

$$c_{q} = \frac{1}{NV} \frac{\partial}{\partial T} \left(\frac{\omega_{q}}{exp\left(\frac{\omega_{q}}{k_{b}T}\right) - 1} \right),$$

where N is the total number of grid points in the reciprocal space; V is the volume of the unit cell; ω_q is magnon frequency at grid point q, k_b is the Boltzmann constant and T is the temperature. ω_q, c_q, v_q are obtained from the calculated magnon dispersions (see SI note 2), which show great agreement with experimental data at 10 K (SI Fig. S3).

The magnon thermal conductivity was obtained based on the lifetime calculated from the magnon linewidth. The magnon linewidths were obtained by fitting experimental and calculated (see SI note 2) one-dimensional dynamic structure factor S(E) slices at $\mathbf{Q}_1=(0.5,0.5,3)$ and $\mathbf{Q}_2=(1.75,1.75,1.75)$. The experimental data were fitted with a convolution of the resolution and the intrinsic lifetime broadening. The

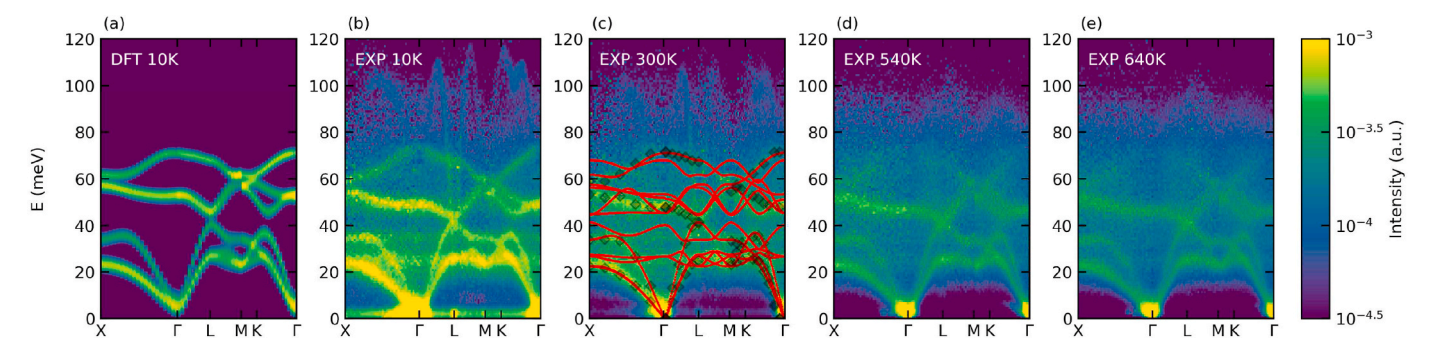


Fig. 1. Folded spectrums of the experimental and calculated INS dynamic structure factor S (O.E). Data folding was done by integrating the intensity of INS over 100 slices, which have data coverages greater than 70%, into an irreducible wedge. (a) Folded coherent one-phonon scattering S (Q,E) simulation at 10 K with the same Q integration configurations as experimental ones. (b-e) Experimental S (Q,E) at 10, 300, 540 and 640 K. Previous phonon dispersion measurements at 300 K [57] and calculated phonon dispersions are plotted in (c) as black dots and red curves, respectively. Thermal occupation corrections were applied to both the calculated and experimental data.

resolution function is Gaussian and its linewidth, Γ_G , includes contributions from the instrument energy and Q resolution. A Lorentzian function with its half-width half-maximum (HWHM), Γ_L , is used for the intrinsic lifetime broadening. For 10 K, the fitted Γ_L are 1.9 $\pm~$ 0.5 and 1.7 ± 0.8 meV and magnon intrinsic lifetime, $au = \frac{1}{2\Gamma_1}$, are 172 and 191 fs at Q_1 and Q_2 , respectively. The results on magnon lifetimes are comparable with previous measurements on ultrathin ferromagnetic films using spin-polarized high-resolution electron energy loss spectroscopy [60]. As suggested by Wu et al. [59], magnon lifetimes τ_a scale with ω_a^{-1} in the presence of spin-phonon interactions, hence, τ_q can be approximated by $\tau_q = \tau_0 \omega_0 / \omega_q$, in which τ_0 and ω_0 are the magnon energy and lifetime at the top of the dispersion. Although NiO has two magnon eigenmodes, they degenerate in a wide span of reciprocal space. The degeneracy is broken only in the vicinity of the magnetic zone center with magnon gaps of 4.3 and 0.6 meV [61,62]. In this case, the effect of the magnon gap on magnon transport was not considered. With specific heat, the projected group velocity and the lifetime obtained at 10 K, κ_m along [1,0,0] direction is calculated to be 0.2, 0.9, 1.3 $W/(m \cdot K)$ at 100, 300, 500 K respectively, as shown in Fig. 3 d. It should be noted that the temperature dependences of magnon τ_q and ω_q are not considered in the present calculation and the κ_m should be treated as an upper limit because both τ_q and ω_q decrease with temperature (Fig. 2). At 300 K, the magnon intrinsic linewidth Γ_L are 5.7 \pm 1.0 and 6.4 \pm 0.8 meV and magnon intrinsic lifetime, are 58 and 51 fs at Q_1 and Q_2 , respectively (Fig. 2 a,b). At 300 K, the calculated magnon thermal conductivity is around 0.3 $W/(m \bullet K)$ and much less than the upper limit. We estimated the κ_m between 10 and 500 K using temperature-dependent magnon energies and lifetimes, which are obtained from linear fittings of the experimental data at 10 and 300 K. As shown in Fig. 3 d, the estimated

 κ_m first increases from 10 to 320 K and gradually decrease above 320 K. The phonon thermal conductivity (κ_p) was calculated based on 3-

phonon scattering with the single mode relaxation time (SMRT) approximation [55,56] (see Sec. 2.2.1). Phonon-isotope scattering due to the mass variance of isotope distributions was also considered (see Sec. 2.2.1). Phonon-defect scattering due to point defects was estimated by fitting TDTR data below 200 K (see Sec. 2.2.1). The calculated κ_n using SMRT approximation and direct solution of the linearized Boltzmann transport equation (LBTE) shows little difference (SI Fig.S4). It should be mentioned that other calculational results of κ_D obtained by direct solution of LBTE with considered phonon-phonon and phonon-isotope scattering have recently been reported [35]. The reported κ_p is around 25 $W/(m \cdot K)$ at 300 K, much lower than our calculation (natural with defect, 31 $W/(m \cdot K)$) and our measurement (30 $W/(m \cdot K)$) shown in Fig. 3 d. The difference may arise from the different exchange-correlation functionals that were used (LDA in the present work, hybrid-PBE in Ref. [35]) and the difference in phonon dispersion (~7% in the total energy scale). Above 200 K, the calculated κ_p follows T^{-1} (Fig. 3 d), which is typical for nonmetallic materials in high-temperature regimes due to phonon-phonon interactions [63].

The calculated thermal conductivity of the phonons is much larger than that of the magnons in the AFM phase (Fig. 3 d). The total thermal conductivity is determined mainly by phonon transport. The huge difference between κ_D and κ_m mainly results from the difference in cumulative specific heat, where the specific heat of magnons is about two orders of magnitude lower than that of phonons at 100 K (Fig. 3 b). Near and above T_N, magnon lifetimes are expected to decrease drastically due to the loss of long-range spin order, and the thermal conductivity by magnon is also expected to be small.

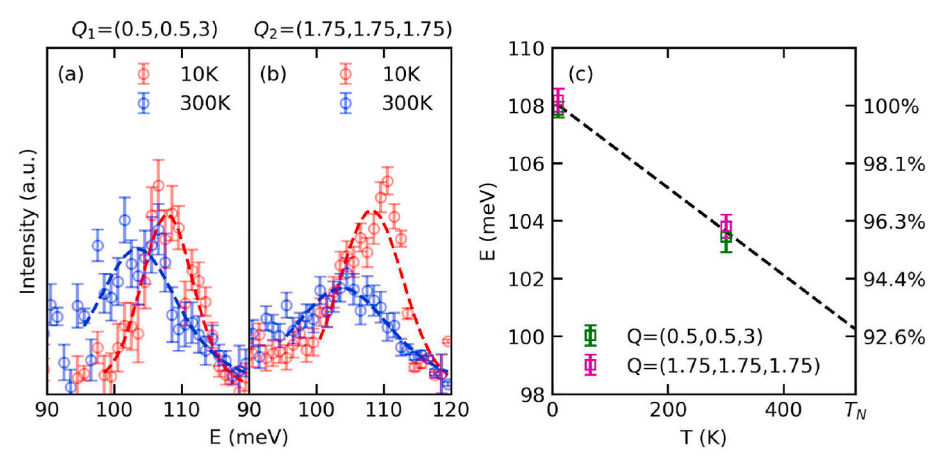


Fig. 2. Temperature dependence of magnon energy at $Q_1 = (0.5,0.5,3)$ and $Q_2 = (1.75,1.75,1.75)$. (a, b) Fitting of the experimental data at Q1 and Q2 with a Q integration range of ± 0.1 (r.l.u.). Red and blue circles are experimental data at 10, 300 K, respectively. Error bars denote statistical errors. Dashed lines are the fitting results (see text) by the Voigt function with fixed Gaussian linewidth obtained from the fitting magnon S (Q,E) calculation at 10, 300 K, respectively. The energy of the magnon decreases with temperature. The green and purple squares are centers of the fitted peaks at Q1 and Q2, and the error bars denote the fitting errors.

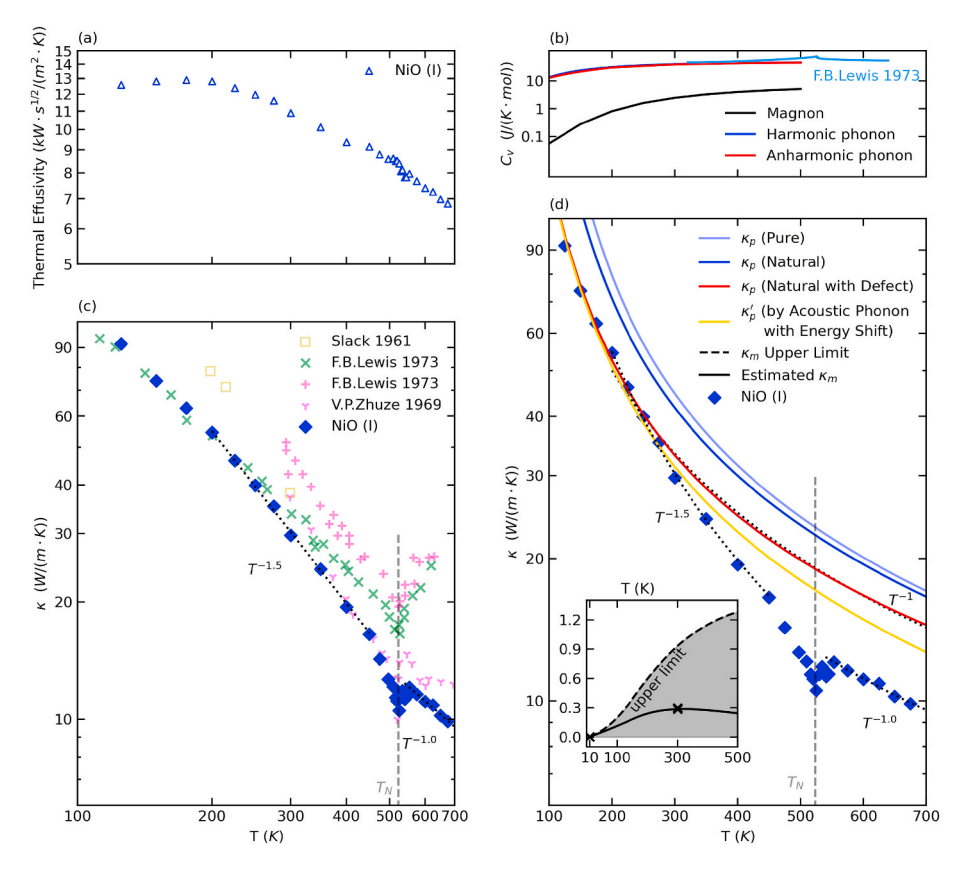


Fig. 3. Temperature-dependent experimental and calculated thermal properties of NiO. (a)Thermal effusivity of NiO (I) measured by TDTR. (b) Calculated specific heat of magnons and phonons. The blue (red) curves indicate the calculated specific heat of the harmonic (anharmonic) phonons. The calculated specific heat agrees well with previously measured data around 400 K [32]. The black curve indicates the calculated specific heat of the magnon. (c,d) Experimental and calculated thermal conductivity. The blue squares show the thermal conductivity results for NiO (I) from the TDTR measurement. In panel (c), purple, green, vellow and pink labels show previous thermal conductivity measurements on NiO [30-32]. In panel (d), the blue (light blue) lines indicate the calculated thermal conductivity of phonon κ_p based on 3-phonon scattering of natural (pure) compounds. The κ_n of natural compounds includes the effect from phonon-isotope scattering due to the mass variance of natural isotope distributions. The red line shows the estimation of the κ_p by phonon-phonon, phonon-isotope, and phonon-defect scattering. The yellow line shows the $\kappa_p^{'}$ by acoustic phonon modes considering phonon energy shifts with temperature (see text). Data points are fitted using different temperature dependences as indicated by the black dotted lines (see text). In the inset, the black dashed curve indicates the calculated upper limit of κ_{m} and the solid shows the estimated temperature-dependent magnon energies and lifetimes. The black cross labels indicate κ_{m} calculated at 10 K and 300 K

TDTR measurements were performed on two NiO single crystals labelled NiO (I) and NiO (II) (see Sec. 2.1.2). TDTR is a transient method for thermal transport measurements whose experimental signals are proportional to thermal effusivity ($\sqrt{\kappa C}$). The NiO (I) crystal has a flat thermal effusivity below 200 K. Above 200 K, the thermal effusivity decreases with temperature, and a small dip was observed at 523 K. Using values from the literature for the heat capacity versus temperature of NiO [32,44] (see SI Fig. S5), we estimate the thermal conductivity versus temperature from the experimentally measured thermal effusivities.

The thermal conductivity of NiO (I) in the AFM phase depends strongly on temperature between 200 and 450 K κ decreases from 55 $W/(m \bullet K)$ at 200 K to 17 $W/(m \bullet K)$ at 450 K. This corresponds to a temperature dependence of $T^{-1.5}$ (Fig. 3c). At temperatures greater than 550 K in the PM phase, the temperature dependence of the thermal conductivity is weaker. The thermal conductivity decreases with $T^{-1.0}$ above 550 K. The NiO (II) crystal has lower thermal conductivity with weaker temperature dependence (Fig.S11) because of a higher defect concentration than NiO (I). κ of NiO (I) in Fig. 3c is more representative of the intrinsic transport properties of NiO.

We now compare our results to prior measurements of κ of NiO. Our data show a trend similar to previous results measured by Zhuze et al. using a pulse technique [31], see Fig. 3c. Both measurements show an overall decreasing thermal conductivity with temperature, with a dip around T_N . Although our data are consistent with the results by Lewis et al. [32] below 200 K, the measured thermal conductivity is lower and shows a stronger temperature dependence from 200 to 450 K (Fig. 3 c). The discrepancy may be related to radiation heat loss in the steady-state longitudinal method used [32,64], see SI Fig.S6. Errors in thermal conductivity caused by heat loss from radiation are known to follow the T^3 dependence [64]. We calculate the difference between our measurements and the steady-state results ($\Delta \kappa$) at 200–500 K and find it to be proportional to T^3 (see SI Fig. S6).

In Fig. 3d, we compare our experimental and theoretical predictions

for the thermal conductivity. While the calculated κ_{D} (natural with defect) and the measured κ are in good agreement for T < 300 K, they diverge for T above room temperature. Experimental κ decreases more rapidly with T than theory can explain. The discrepancy between theory and experiment increases as T increases from 300 to $T_N = 523$ K. Then, at temperatures above T_N , the difference between experimental and theoretical κ stays roughly constant at ~25%. In addition to disagreeing with our theoretical predictions for NiO, we note that a $T^{-1.5}$ dependence for κ is different from other non-magnetic insulators with face-center-cubic crystal structure and similar phonon properties. For example, crystals such as MgO have a κ that is proportional to T^{-1} (SI Fig.S7) in the same temperature range. Therefore, we conclude that simple phonon-phonon scattering, or phonon-isotope and phonon-defect scattering, cannot explain the observed temperature dependence of NiO at 200-450 K (Fig. 3 d). We conclude that there is another temperature-dependent scattering term that affects transport at temperatures above 300 K.

In kinetic theory, temperature effects on phonon transport can be reflected in two parts: changes in phonon energy and lifetime. On one hand, the shift in phonon energy affects thermal capacity (unless the temperature is well above Debye temperature) and group velocity, and thus thermal conductivity. From our INS measurements on polycrystalline NiO, the measured phonon energies monotonically decrease with temperature for both TA and LA modes (Fig. 4 a, b), and for optical modes (SI Fig.S1). The softening of acoustic phonon energy with temperature was also observed via INS measurements on single crystal NiO, as shown in Fig. 4 c-e. With the assumption of isotropic and uniform softening of the phonon modes on heating, the phonon energy for the specific phonon mode i at temperature T can be approximated by $\omega_i(T) = \omega_{0i}(1 - \eta T)$, where ω_{0i} is the phonon energy at 0 K, η is a positive coefficient representing softening of the acoustic phonon mode i and is obtained from linear fittings $\omega = \omega_0(1 - \eta T)$ on the measured phonon energy (Fig. 4 a, b). The obtained η_{TA} and η_{LA} are 5.6×10^{-5} and $4.5 \times 10^{-5} K^{-1} meV^{-1}$, respectively. In the long wavelength limit, the group velocity for mode *i* can be expressed as $v_i = v_{0i}(1 - \eta T)$. The effect

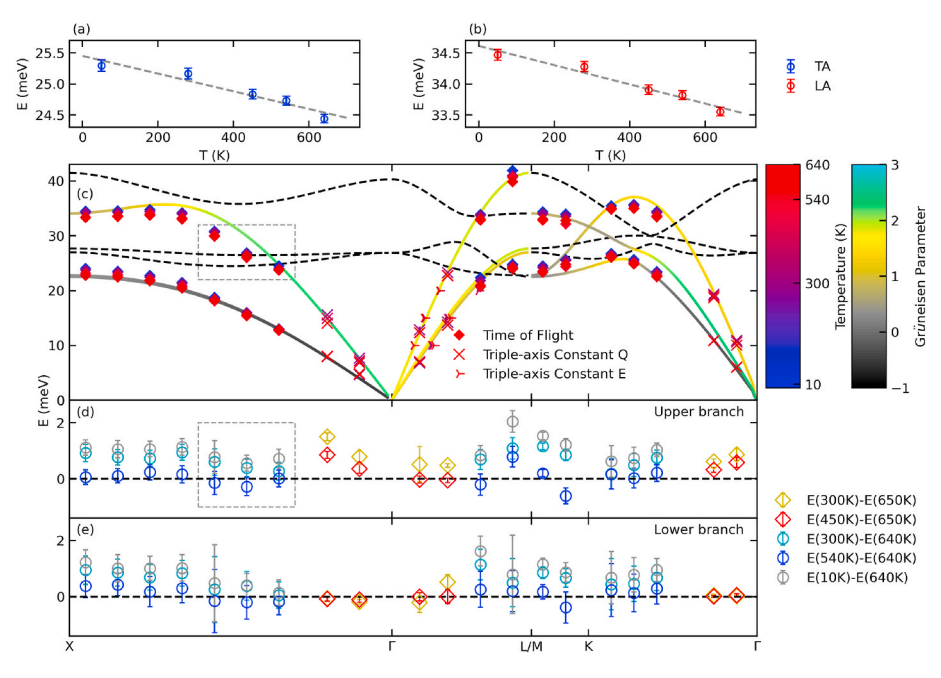


Fig. 4. Temperature-dependent phonon energy variations from INS experiments. (a,b) Phonon energies from the phonon density of state INS measurements with incident neutron energy of 50 meV at 50, 280, 450, 540 and 640 K. The experimental data have been corrected for by multiphonon scattering and thermal occupation. There are two distinct peaks around 25 and 34 meV, corresponding to the (a) TA and (b) LA phonon modes. (c) Measured and calculated phonon energies for LA and TA modes along high-symmetry directions. Squares and cross markers represent phonon energies from the time-of-flight (measured at 10, 300, 540 and 640 K) and triple-axis (measured at 300, 450 and 650 K) INS measurements, and the corresponding colors denote temperatures. The qresolved mode Grijneisen parameters are calculated based on quasi-harmonic approximation and indicated by the colored lines. Zone-folding modes that cannot be seen from INS experiments are shown in dashed lines. The fitting errors are smaller than the marker size. (d,e) Difference of the phonon energy from low to high temperature of the upper branch (d) and the lower branch (e). All phonon energies were extracted from Lorentzian fittings of the measured data, and error bars indicate fitting errors. The incoherent INS scattering signals around 26 meV can cause slightly biased phonon energies, as denoted by grev boxes.

of phonon softening on mode thermal conductivity can be shown by $\zeta_i(T) = \frac{c_i(T) v_i(T)^2}{(c_i(T) v_i(T)^2)|_{\eta=0}}, \text{ where } c_i(T) = \frac{1}{V} \frac{\partial}{\partial T} \frac{\omega_{0i}(1-\eta T)}{\exp\left(\frac{\omega_{0i}(1-\eta T)}{k_h T}\right) - 1}.$

Assuming that the phonon lifetime does not change, the thermal conductivity with temperature-induced acoustic phonon energy shifts was calculated as

$$\kappa_{p}^{'}(T) = \sum_{qj} \kappa_{p,qj} \zeta_{qj}(\eta,T)$$

$$= \sum_{qj} c_{p,qj} v_{p,qj}^2 |_{\eta=0} \zeta_{qj}(\eta, T) \tau_{p,qj},$$

in which $\kappa_{p,qj}$ represents the calculated mode thermal conductivity for specific phonon mode at point q for branch j, and the softening coefficient η was set to be η_{TA} for all acoustic phonon modes. The group velocities (Fig. 1) and lifetimes (SI Fig.S2 a) of the acoustic phonon modes are much larger than those of the optical modes, and the acoustic phonon modes contribute more than 90% of the total thermal conductivity at 300–700 K (SI Fig.S2 b). In this case, the κ_p' can be approximated by considering only acoustic phonons. As shown in Fig. 3 d, the κ_p' is not sufficient to explain the $T^{-1.5}$ temperature dependence, although it was underestimated due to the exclusion of optical phonon transport, the approximation of group velocities in long wavelength limit, and the use of a large softening coefficient η for all acoustic modes.

In our discussion above, we have ruled out phonon-isotope scattering, phonon-defect scattering, and phonon softening as explanations for the κ vs. T dependence of NiO. We now turn our attention to spin-phonon interactions that affect phonon lifetime. In magnetic insulators, magnon-phonon scattering (MPS) can also affect phonon transport. According to Matthiessen's rules, the scattering rate for the specific phonon mode i is expressed by

$$\tau_{p,i}^{-1} = \tau_{pp,i}^{-1} + \tau_{pi,i}^{-1} + \tau_{pd,i}^{-1} + \tau_{mp,i}^{-1},$$

where $\tau_{pp,i}^{-1}$, $\tau_{pd,i}^{-1}$, $\tau_{pd,i}^{-1}$, $\tau_{mp,i}^{-1}$ correspond to the scattering rate for phonon-phonon, phonon-isotope, phonon-defect, and magnon-phonon scattering processes.

Spin-phonon interactions will have two effects on thermal transport.

First, MPS $(\tau_{mp,i}^{-1})$ will reduce the phonon lifetimes. The single-mode acoustic phonon scattering rate can be expressed by $\tau_{mp,i}^{-1} = nv_s\sigma$, where n is the density of scatters, v_s is the speed of sound, σ is the scattering cross section [65]. In this simplified MPS model, the temperature dependences of σ can be described by $\sigma = \pi(\lambda(T)/2)^2$ [12]. where $\lambda(T)$ is the magnetic correlation length. We approximate the correlation length from the HWHM $(\Theta_{me}(T))$ of magnetic elastic Bragg peak (Fig. 5 a) by $\lambda(T) = 1/\Theta_{me}(T)$. Noting that the $\lambda(T)$ is underestimated due to the instrument resolution in \mathbf{Q} (~ 0.04 Å). For phonons scattered by magnon mode, $n = \int n_{BE}(E, T)g_m(E)dE$, where n_{BE} is Bose-Einstein statistics, E is magnon energy and $g_m(E)$ is the magnon density of state. With a fixed v_s , the normalized single phonon scattering rates $au_{mp,i}^{-1}(T)/ au_{mp,i}^{-1}(450~K)$ first increases slowly then dramatically from 0 to 450 K (Fig. 5 b). The $au_{mp,i}^{-1}$ at 200 K is only 8% of the $au_{mp,i}^{-1}$ at 450 K, hence, the magnon-phonon scattering is less important at low temperatures. At 200–450 K, $\tau_{mp.i}^{-1}$ is of a higher order of T and can lead to the observed strong temperature dependence of thermal conductivity. We note that fully quantifying the contribution of MPS to thermal conductivity requires a detailed calculation of the phase space and interaction strength (collision matrix) of MPS. This is beyond the scope of the current work.

Second, spin-phonon interactions break the symmetry of the phonon system dynamically, leading to increases in the phonon-phonon scattering strength $(\tau_{vv,i}^{-1})$. Recently, we reported neutron scattering signatures of acoustic phonon eigenvector renormalizations in NiO [29]. The eigenvectors of transverse acoustic phonons are renormalized to a lower symmetry (as shown in SI Fig.S8), resulting in INS intensities 'forbidden symmetry'. The renormalizations are not caused magnetostriction-induced static lattice distortion. Instead, they originate from spin-phonon interactions, which dynamically break the symmetry of the phonons. Because the selection rules for phonon-phonon scattering depend on the symmetry of phonon eigenvectors [66], eigenvector renormalizations could affect phonon transport. Generally, higher symmetry imposes more restrictions (additional selection rules) on the phonon-phonon scattering process, resulting in weaker phonon-phonon interaction strength and therefore higher thermal conductivity [66]. On the contrary, dynamic symmetry breaking of

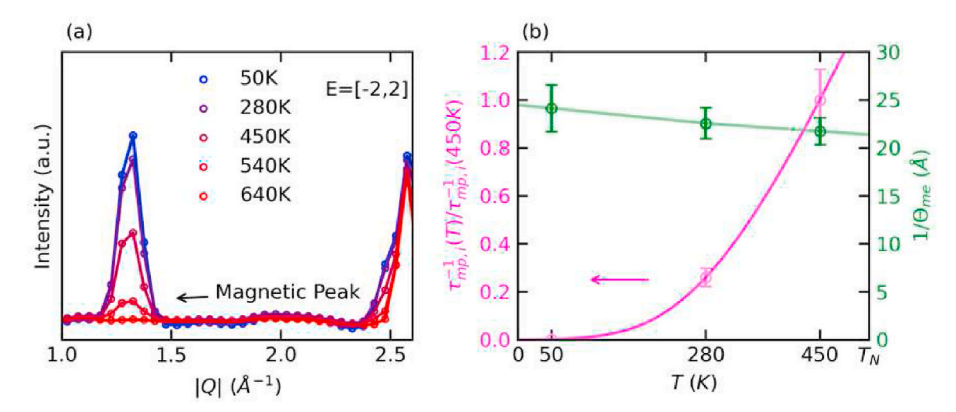


Fig. 5. Sketch of the phonon scattering rate in the MPS process. (a) One-dimensional S (|Q|) by INS powder measurements at 50–640 K with energy integration of ± 2 meV. The elastic magnetic peaks show around 1.3 Å $^{-1}$ and their intensities weaken on heating significantly, whereas elastic lattice peaks retain the same. (b) The inverse of the HWHM of the magnetic elastic Bragg peak $1/\theta_{me}(T)$ (green labels) and normalized phonon scattering rate $\tau_i^{-1}(T)/\tau_i^{-1}(450~K)$ (purple labels). Colored lines are guides for the eye.

the phonon system leads to a stronger phonon-phonon interaction strength, and thus lower thermal conductivity in NiO. This effect is not included in the calculated κ_p due to its dynamic nature.

Near T_N (450–550 K), the kink in the heat capacity is a measure of the entropy in the lattice and spin system due to the phase transition. Because the measured thermal effusivity shows no kink there, the increase in heat capacity (caused by an increase in disorder through the phase transition) is compensated by a corresponding decrease in thermal conductivity. This suggests that the average phonon lifetime is inversely proportional to the disorder in the spin system. The dip in thermal conductivity is attributed to critical magnetic fluctuation-phonon scattering [67].

The measured thermal conductivity shows a weaker temperature dependence of $T^{-1.0}$ above T_N . It has been shown that the slight structural distortion from magnetostriction hardly affects the thermal conductivity by phonon transport in NiO [35]. The measured κ is still lower than the calculated κ_p (natural isotope with defects) at 550–700 K, suggesting that the effects from spin-phonon interactions may still be significant above T_N . This is expected because paramagnons (SI Fig.S3) and phonon eigenvector renormalizations [29] are observed in this temperature range. As a result, the effects from magnon-phonon scattering and spin-induced dynamic symmetry breaking do not vanish. Although there is no long-range spin order in this state, a short-range spin order exists and may give rise to the spin-phonon interaction. Suppression of thermal conductivity by spin-phonon interactions was also found previously in other materials in the PM state [10,68].

Generally, one would expect the melting of antiferromagnetic order to do one of two things to magnon-phonon scattering rates above the T_N. Either, magnon-phonon scattering rates would saturate, i.e. stop increasing with temperature because the entropy in the spin system has been maximized. Or, magnon-phonon scattering would vanish due to the lack of antiferromagnetic order. If the magnon-phonon scattering rates saturate, i.e., $\tau_{mp,i}^{-1}$ became temperature independent above T_N , then the above expression for thermal conductivity predicts a T^{-n} dependence with n < 1, like is observed in insulating crystals with significant crystalline disorder. Alternatively, if magnon-phonon scattering vanishes due to the lack of spin order, then the thermal conductivity should recover. These seem contradict the observed temperature dependence. In the present case, we observed the existence of paramagnon above T_N below 640 K (SI Fig.S3). This indicates that magnetic entropy is not yet maximized in this temperature range, and strong short-range spin correlations give rise to coherent paramagnons. The paramagnon-phonon scattering may contribute to the suppression of thermal conductivity above T_N.

Another possible mechanism for the observed temperature dependence above T_N is that changes in the antiferromagnetic order lead to changes in phonon-phonon scattering rates. This could occur for several reasons. One possibility is spin-disorder effects bonding [69], which could lead to an increase in anharmonicity. To explore the effect of spin

order on phonon anharmonicity, we calculated the phonon properties with ferromagnetic (FM) spin order to understand the effects of magnetic order (see Method Sec. 4.2.1). The obtained phonon mode Grüneisen parameters (SI Fig. S9) as well as temperature-dependent mode energies (SI Fig. S10) show only minor changes compared with those in the AFM state. However, we note that the temperature dependence of the INS measured phonon frequencies is higher near the $T_{\rm N}$ than what our calculations for NiO in the AFM or FM state predict. Thus, the spin-phonon interaction on the phonon thermal conductivity can be indirect: melting of the spin order causes changes in phonon anharmonicity, which leads to larger phonon-phonon scattering rates in the PM vs. AFM phase.

The TA, LA, TO, LO decrease in energy of 3%, 3%, 5%, 4% from 50 to 640 K, respectively (Fig. 4 a,b & Fig.S1 c,d). We calculated the 3-phonon scattering phase space at 0 and 640 K and found that the phonon-phonon scattering phase space changes little (see Fig.S12). Therefore, temperature-dependent DFT such as molecular dynamics calculations shall not change the results significantly.

4. Conclusions

In summary, by performing INS and TDTR thermal conductivity measurements and atomistic thermal conductivity calculations, spinphonon interactions are identified as the origin of strong temperature dependence of thermal conductivity in the AFM phase. Using the extrapolated magnon lifetime from INS measurements, the magnon thermal conductivity is estimated to be more than one order of magnitude smaller than its phonon counterpart in the temperature range studied. In the AFM phase, the measured thermal conductivity at 200–450 K shows a strong temperature dependence of $T^{-1.5}$. We ruled out phonon-isotope scattering, phonon-defect scattering, and phonon softening as the source of the anomalous temperature dependence. The stronger temperature dependence is attributed to magnon-phonon scattering and spin-induced dynamic symmetry breaking. Our results provide a detailed study of thermal transport in this important material, highlighting the pivotal role of spin-phonon interactions in lattice thermal transport. Similar interactions and their effects may play significant roles in thermal transport in other materials where spin and lattice degrees of freedom are strongly coupled. The results shed light on controlling thermal transport through spin-phonon interactions and engineering functional antiferromagnetic spintronics materials through these interactions.

Declaration of competing interest

The authors declare that they have no known competing financial interests or personal relationships that could have appeared to influence the work reported in this paper.

Data availability

Data will be made available on request.

Acknowledgements

Q.S., Y.S., S.H. and C.L. are supported by the National Science Foundation under Grant No 1750786. S.H. and R.W. are supported by the National Science Foundation under Grant No. 1847632, and by the Army Research Office under Grant No. W911NF-18-1-0364 and No. W911NF-20-1-0274. This research used resources at the Spallation Neutron Source, a DOE Office of Science User Facility operated by the Oak Ridge National Laboratory. A part of this research was undertaken on the TAIPAN beamline at OPAL reactor, ANSTO.

Appendix A. Supplementary data

Supplementary data to this article can be found online at https://doi. org/10.1016/j.mtphys.2023.101094.

References

- [1] R.L. Douglass, Heat transport by spin waves in yttrium iron garnet, Phys. Rev. 129 (3) (1963) 1132-1135.
- C. Hess, et al., Magnon heat transport in doped La2CuO4, Phys. Rev. Lett. 90 (19) (2003): 197002.
- [3] R. Jin, et al., In-plane thermal conductivity of Nd2CuO4: evidence for magnon heat transport, Phys. Rev. Lett. 91 (14) (2003): 146601.
- [4] B.Y. Pan, et al., Specific heat and thermal conductivity of ferromagnetic magnons in Yttrium Iron Garnet, EPL 103 (3) (2013): 37005.
- [5] N. Prasai, et al., Ballistic magnon heat conduction and possible Poiseuille flow in the helimagnetic insulator Cu2OSeO3, Phys. Rev. B 95 (22) (2017): 224407.
- [6] G.S. Dixon, Lattice thermal conductivity of antiferromagnetic insulators, Phys. Rev. B 21 (7) (1980) 2851-2864.
- [7] G. Laurence, D. Petitgrand, Thermal conductivity and magnon-phonon resonant interaction in antiferromagnetic FeCl2, Phys. Rev. B 8 (5) (1973) 2130-2138.
- [8] B. Wei, et al., Phonon anharmonicity: a pertinent review of recent progress and erspective, Sci. China Phys. Mech. Astron. 64 (11) (2021): 117001.
- S. Bao, et al., Evidence for magnon-phonon coupling in the topological magnet Cu3TeO6, Phys. Rev. B 101 (21) (2020): 214419.
- [10] C.A. Pocs, et al., Giant thermal magnetoconductivity in CrCl3 and a general model for spin-phonon scattering, Physical Review Research 2 (1) (2020): 013059.
- [11] D.R. Ratkovski, et al., Thermal transport in yttrium iron garnet at very high magnetic fields, Phys. Rev. B 101 (17) (2020): 174442.
- [12] P.A. Sharma, et al., Thermal conductivity of geometrically frustrated, ferroelectric YMnO3: extraordinary spin-phonon interactions, Phys. Rev. Lett. 93 (17) (2004):
- [13] F. Meier, J. Levy, D. Loss, Quantum computing with antiferromagnetic spin clusters, Phys. Rev. B 68 (13) (2003): 134417.
- [14] O. Gomonay, T. Jungwirth, J. Sinova, High antiferromagnetic domain wall velocity induced by neel spin-orbit torques, Phys. Rev. Lett. 117 (1) (2016): 017202.
- [15] C. Tzschaschel, et al., Ultrafast optical excitation of coherent magnons in antiferromagnetic NiO, Phys. Rev. B 95 (17) (2017): 174407.
- [16] M. Fechner, et al., Magnetophononics: ultrafast spin control through the lattice, Physical Review Materials 2 (6) (2018): 064401.
- Y.W. Windsor, et al., Exchange-striction driven ultrafast nonthermal lattice [17] dynamics in NiO, Phys. Rev. Lett. 126 (14) (2021): 147202.
- Г181 T. Jungwirth, et al., Antiferromagnetic spintronics, Nat. Nanotechnol. 11 (3) (2016) 231–241.
- [19] G.E. Bauer, E. Saitoh, B.J. van Wees, Spin caloritronics, Nat. Mater. 11 (5) (2012) 391_399.
- [20] S.R. Boona, R.C. Myers, J.P. Heremans, Spin caloritronics, Energy Environ. Sci. 7 (3) (2014) 885.
- [21] H. Wang, et al., Antiferromagnonic spin transport from Y3Fe5O12 into NiO, Phys. Rev. Lett. 113 (9) (2014): 097202.
- [22] C. Hahn, et al., Conduction of spin currents through insulating antiferromagnetic oxides, EPL 108 (5) (2014): 57005.
- [23] H. Wang, et al., Spin transport in antiferromagnetic insulators mediated by magnetic correlations, Phys. Rev. B 91 (22) (2015); 220410.
- T. Shang, et al., Effect of NiO inserted layer on spin-Hall magnetoresistance in Pt/ **[24]** NiO/YIG heterostructures, Appl. Phys. Lett. 109 (3) (2016): 032410.
- Γ251 M. Foëx, A type of transformation common to manganous, ferrous, cobaltous, and nickelous oxides, Compt. rend 227 (1948) 193-194.
- J.R. Tomlinson, et al., The high temperature heat content of nickel oxide, J. Am. Chem. Soc. 77 (4) (1955) 909-910.
- H. Kondoh, et al., Magnetic anisotropy measurements of NiO single crystal, J. Phys. Soc. Jpn. 13 (6) (1958) 579-586.
- N.P. Duong, T. Satoh, M. Fiebig, Ultrafast manipulation of antiferromagnetism of **[28]** NiO, Phys. Rev. Lett. 93 (11) (2004): 117402.

- [29] Q. Sun, et al., Mutual spin-phonon driving effects and phonon eigenvector renormalization in nickel (II) oxide, Proc. Natl. Acad. Sci. USA 119 (29) (2022) e2120553119.
- [30] G.A. Slack, R. Newman, Thermal conductivity of MnO and NiO, Phys. Rev. Lett. 1 (10) (1958) 359–360.
- [31] V. Zhuze, N. On, A. Shelykh, Thermal conductivity near a continuous phase transition, SOVIET PHYSICS SOLID STATE, USSR 11 (5) (1969) 1044
- [32] F.B. Lewis, N.H. Saunders, The thermal conductivity of NiO and CoO at the Neel temperature, J. Phys. C Solid State Phys. 6 (15) (1973) 2525-2532.
- [33] J. Keem, J. Honig, Selected Electrical and Thermal Properties of Undoped Nickel Oxide, 1978.
- [34] M. Massot, et al., Critical behavior of CoO and NiO from specific heat, thermal conductivity, and thermal diffusivity measurements, Phys. Rev. B 77 (13) (2008).
- [35] J. Linnera, A.J. Karttunen, Lattice dynamical properties of antiferromagnetic MnO, CoO, and NiO, and the lattice thermal conductivity of NiO, Phys. Rev. B 100 (14) (2019): 144307.
- [36] E. Aytan, et al., Spin-phonon coupling in antiferromagnetic nickel oxide, Appl. Phys. Lett. 111 (25) (2017): 252402.
- [37] O. Arnold, et al., Mantid-data analysis and visualization package for neutron scattering and μ SR experiments, Nucl. Instrum. Methods Phys. Res. Sect. A Accel. Spectrom. Detect. Assoc. Equip. 764 (2014) 156-166.
- [38] GETDOS. Available from: https://code.google.com/archive/p/getdos/.
- [39] D.G. Cahill, Analysis of heat flow in layered structures for time-domain thermoreflectance, Rev. Sci. Instrum. 75 (12) (2004) 5119-5122.
- [40] J.P. Perdew, K. Burke, M. Ernzerhof, Generalized gradient approximation made simple, Phys. Rev. Lett. 77 (18) (1996) 3865-3868.
- J.P. Feser, D.G. Cahill, Probing anisotropic heat transport using time-domain thermoreflectance with offset laser spots, Rev. Sci. Instrum. 83 (10) (2012): 104901
- [42] C. Thomsen, H.J. Maris, J. Tauc, Picosecond acoustics as a non-destructive tool for the characterization of very thin films, Thin Solid Films 154 (1) (1987) 217-223.
- [43] D.A. Ditmars, C.A. Plint, R.C. Shukla, Aluminum. I. Measurement of the relative enthalpy from 273 to 929 K and derivation of thermodynamic functions for Al(s) from 0 K to its melting point, Int. J. Thermophys. 6 (5) (1985) 499–515.
- [44] H. Seltz, B.J. DeWitt, H.J. McDonald, The heat capacity of nickel oxide from 68-298°K. And the thermodynamic properties of the oxide, J. Am. Chem. Soc. 62 (1) (1940) 88-89.
- [45] D.S. Kim, et al., Nuclear quantum effect with pure anharmonicity and the anomalous thermal expansion of silicon, Proc. Natl. Acad. Sci. U. S. A. 115 (9) (2018) 1992-1997.
- [46] G. Kresse, J. Furthmüller, Efficient iterative schemes for ab initio total-energy calculations using a plane-wave basis set, Phys. Rev. B 54 (16) (1996) 11169-11186.
- [47] G. Kresse, J. Furthmüller, Efficiency of ab-initio total energy calculations for metals and semiconductors using a plane-wave basis set, Comput. Mater. Sci. 6 (1) (1996) 15-50.
- [48] P.E. Blochl, Projector augmented-wave method, Phys. Rev. B Condens, Matter 50 (24) (1994) 17953-17979
- G. Kresse, D. Joubert, From ultrasoft pseudopotentials to the projector augmentedwave method, Phys. Rev. B 59 (3) (1999) 1758-1775.
- [50] J.P. Perdew, A. Zunger, Self-interaction correction to density-functional approximations for many-electron systems, Phys. Rev. B 23 (10) (1981) 5048-5079
- [51] V.V. Anisimov, J. Zaanen, O.K. Andersen, Band theory and mott insulators: hubbard U instead of stoner I, Phys. Rev. B Condens. Matter 44 (3) (1991) 943-954
- [52] S.L. Dudarev, et al., Electron-energy-loss spectra and the structural stability of nickel oxide: an LSDA+U study, Phys. Rev. B 57 (3) (1998) 1505-1509.
- [53] A.M. Balagurov, et al., Magnetostructural phase transitions in NiO and MnO: neutron diffraction data, JETP Lett. 104 (2) (2016) 88-93.
- [54] A. Togo, I. Tanaka, First principles phonon calculations in materials science, Scripta Mater. 108 (2015) 1-5.
- [55] A. Togo, L. Chaput, I. Tanaka, Distributions of phonon lifetimes in Brillouin zones, Phys. Rev. B 91 (9) (2015): 094306.
- [56] G.P. Srivastava, The Physics of Phonons, Routledge, 2019.
 [57] W. Reichardt, V. Wagner, W. Kress, Lattice dynamics of NiO, J. Phys. C Solid State Phys. 8 (23) (1975) 3955-3962.
- Z. Yamani, et al., Magnetic excitations of spin and orbital moments in cobalt oxideSpecial issue on Neutron Scattering in Canada, Can. J. Phys. 88 (10) (2010) 729_733
- [59] X. Wu, Z. Liu, T. Luo, Magnon and phonon dispersion, lifetime, and thermal conductivity of iron from spin-lattice dynamics simulations, J. Appl. Phys. 123 (8) (2018): 085109.
- [60] H.J. Qin, et al., Temperature dependence of magnetic excitations: terahertz magnons above the curie temperature, Phys. Rev. Lett. 118 (12) (2017): 127203.
- M. Grimsditch, L.E. McNeil, D.J. Lockwood, Unexpected behavior of the antiferromagnetic mode of NiO, Phys. Rev. B 58 (21) (1998) 14462-14466.
- [62] T. Kampfrath, et al., Coherent terahertz control of antiferromagnetic spin waves, Nat. Photonics 5 (1) (2010) 31–34.
- C. Kittel, P. McEuen, P. McEuen, Introduction to Solid State Physics, vol. 8, Wiley, New York, 1996.
- [64] D.G. Cahill, R.O. Pohl, Thermal conductivity of amorphous solids above the plateau, Phys. Rev. B Condens. Matter 35 (8) (1987) 4067-4073.
- J.W. Schwartz, C.T. Walker, Thermal conductivity of some alkali halides containing divalent impurities. II. Precipitate scattering, Phys. Rev. 155 (3) (1967) 969-979

- [66] R. Yang, et al., Crystal symmetry based selection rules for anharmonic phonon-phonon scattering from a group theory formalism, Phys. Rev. B 103 (18) (2021):
- [67] H. Stern, Thermal conductivity at the magnetic transition, J. Phys. Chem. Solid. 26 (1) (1965) 153–161.
- [68] P.V.E. McClintock, I.P. M, R. Orbach, H.M. Rosenberg, The effect of a magnetic field on the thermal conductivity of paramagnetic crystals: holmium ethylsulphate, Proceddings of the Royal Society A 298 (1454) (1967) 359–378.

 [69] L. Mauger, et al., Nonharmonic phonons inα-iron at high temperatures, Phys. Rev.
- B 90 (6) (2014).